

**SPECIAL FEATURE
TUTORIAL**

Gas-phase Reaction Dynamics Studied by Ion Imaging

Liam McDonnell and Albert J. R. Heck*

Department of Chemistry, University of Warwick, Coventry CV4 7AL, UK

Ion imaging is a multiplex detection technique that employs multi-photon ionization and two-dimensional time-of-flight mass spectrometry to obtain detailed information on the dynamics that govern the making and breaking of chemical bonds. It has primarily been used to study gas-phase unimolecular photofragmentations, but can also be used to study bimolecular reactions and photoelectron processes. In many cases ion imaging permits the simultaneous measurement of reaction product branching ratios, quantum-state populations and velocity distributions. © 1998 John Wiley & Sons, Ltd.

J. Mass Spectrom. 33, 415–428 (1998)

KEYWORDS: ion imaging; photodissociation; molecular beams; time-of-flight mass spectrometry; multi-photon ionization; angular distributions; position-sensitive detectors

INTRODUCTION

Ion imaging^{1–6} is a relatively new experimental technique used to study gas-phase uni- and bimolecular reactions at the molecular level. The technique combines resonance-enhanced multi-photon ionization with two-dimensional time-of-flight mass spectrometry using position-sensitive detectors. In gas-phase reaction dynamics, the majority of studies focus on the asymptotic properties of the reactions, measuring product branching ratios, product quantum states and/or velocities (speed and angular distributions). Prior to the development of the ion imaging technique, simultaneous measurement of all these quantities was extremely difficult. However, simultaneous measurement is important so that correlated quantities can be determined, e.g. the velocities of the fragments correlated with the particular quantum states populated. So far the majority of ion imaging experiments have concerned unimolecular photodissociations. More recently, the ion imaging technique has been further extended to investigate bimolecular collision processes^{7–12} and photoelectron processes.^{13–15} Reaction product ion imaging has allowed the simultaneous measurement of integral and differential cross-sections of various benchmark reactions, such as the reactive scattering $H + H_2$ ^{8,9} and $H + HI$ ^{7,12} reactions and the inelastic scattering $Ar + NO$ ^{10,11} reaction. This tutorial paper will focus primarily on the basics of the technique and illustrate its capabilities using a few examples of unimolecular photodissociations.

As for all chemical reactions, photodissociations are governed by the potential energy surfaces the reactions evolve on. In Fig. 1, a schematic representation is given of the potential energy surfaces involved in a 'simple' molecular photodissociation for a hypothetical molecule ABC. The ground-state potential energy surface is termed X and the excited state A, while R is the internuclear distance between atom C and the AB moiety and $h\nu$ is the energy of the laser photon. The ground-

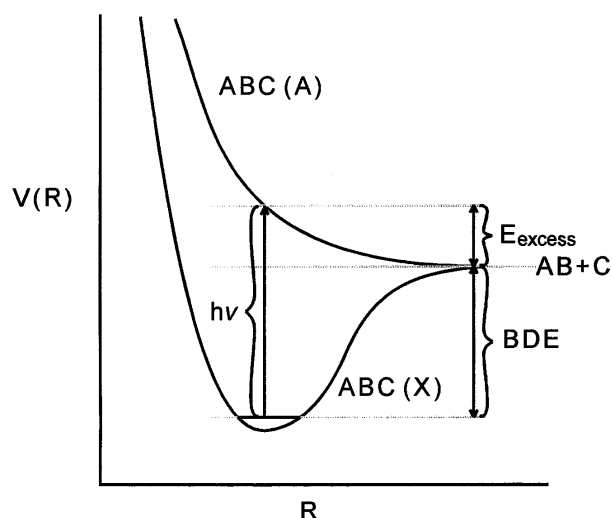


Figure 1. Schematic representation of the photodissociation of a triatomic molecule (ABC). R is the distance between C and the AB diatomic fragment, BDE the bond dissociation energy and $h\nu$ the energy of the photon. Through absorption of a photon the molecule is excited to a repulsive surface via which it dissociates. The excess energy is the energy difference between the photon energy and the bond dissociation energy and it will be distributed among the translational and internal degrees of freedom of the photofragments.

* Correspondence to: A. J. R. Heck, Department of Chemistry, University of Warwick, Coventry CV4 7AL, UK.

state potential energy surface is bound and evolves at long AB–C internuclear distances to an asymptotic energy which corresponds to the energy of the separated AB and C fragments. The energy difference between the ground state of the ABC molecule and the ground state energy of the two AB and C fragments is the bond dissociation energy (BDE). Following absorption of a photon (of energy $h\nu$), the ground-state molecule is, in this case, excited to a repulsive excited state (A). Depending on the repulsive character of the excited state, the molecule will dissociate promptly, or more slowly, into the fragments AB + C. The excess energy, which is the difference between the energy of the photon and the bond dissociation energy, may be distributed among all available degrees of freedom of the nascent fragments (translational and internal). The release of kinetic energy causes the AB and C fragments to move away from the point in space and time where they were generated. The proportion of the excess energy released as kinetic energy and the masses of the AB and C fragments determine their recoil speeds. The residual excess energy is divided over the other degrees of freedom of the fragments and may for instance lead to rotational, vibrational and/or electronic excitation of the fragments. Ion imaging is a multiplex detection technique which allows the *simultaneous* measurement of rotational, vibrational, electronic and translational energy distributions of products of uni- and bimolecular reactions.

In ion imaging, multiplex detection is achieved by combining two more established techniques. The spectroscopic technique resonance-enhanced multi-photon ionization (REMPI) is used to determine product quantum state distributions, and two-dimensional time-of-flight mass spectrometry (using position-sensitive detectors) gives velocity (speed and angular) distributions. The ion images are also sensitive to the alignment of the products (e.g. with respect to the laser polarization vector) and information about such alignment can be obtained from analysis of the data.

Resonance-enhanced multi-photon ionization (REMPI)

When an atom or molecule interacts with a photon of sufficient energy, ionization may occur through removal of an electron. As the ionization potential of most small molecules is above 8 eV, highly energetic photons are required to induce ionization through one-photon absorption. Highly energetic photons can be produced by traditional line sources such as He(I) and Ne(I), which provide radiation of a fixed energy. Tunable radiation may be provided by synchrotron sources and by vacuum ultraviolet (VUV) lasers. In a direct one-photon ionization process there is little state selectivity, i.e. ionization of several vibrational and rotational levels of the electronic ground state occurs to give several electronic, vibrational and rotational levels of the ion, determined mostly by the Franck–Condon factors between the initial and final states.

Most common lasers produce less energetic photons. Visible light lasers (e.g. dye lasers) produce photons of an energy ranging between ~ 1 and 4 eV. The laser photon energy can be extended to higher energies by frequency doubling of the initial light using for instance

non-linear crystals. These photon energies are still insufficient to ionize most molecules. However, the available photon flux of a pulsed dye laser is generally so high that multi-photon absorption can be achieved. In Fig. 2 a schematic diagram is shown of several energy levels of a diatomic molecule AX. The first process (a) shows schematically the one photon ionization of AX by a highly energetic photon. The second process (b) shows the ionization of the same molecule by simultaneous absorption of three photons. This process is far less likely as all photons have to be absorbed simultaneously and it will only occur when the laser flux is sufficiently high. In process (c) the energy of the laser photons are matched to be resonant, at the two-photon level, with an excited state of the neutral molecule. In this process the lifetime of the intermediate state is such that only two photons have to be absorbed simultaneously, making the process more likely than (b). Ionization via a resonant state has been named 'resonance-enhanced multi-photon ionization' (REMPI).¹⁶ The process shown in (c) is termed (2 + 1) REMPI, in which the first integer describes the number of photons required to reach the resonant level and the second integer shows the number of photons required to reach the ionization limit from the resonant level. A particularly useful feature of REMPI is that the resonance wavelength is often different for different quantum states. Therefore, using REMPI each rovibrational level of a molecule can be ionized individually by varying the wavelength of the laser. To illustrate the power of this state-selective ionization, part of a REMPI spectrum of molecular deuterium, adopted from Ref. 17, is shown in Fig. 3. To obtain this spectrum, molecular deuterium was produced via the reaction $D + DI \rightarrow D_2 + I$. This 'hot atom' reaction produces D_2 in a range of vibrational ($0 < v'' < 5$) and rotational levels ($J'' = 0-30$) which, as can be seen in Fig. 3, can be ionized individually by changing the colour (i.e. wavelength) of the ionization laser. For the REMPI spectrum in Fig. 3, ions of m/z 4 (D_2^+ ions) were mass selectively detected as the laser wavelength was scanned. When the individual transition strengths are known, quantitative information regarding product state populations can be obtained from the line intensities in the REMPI spectra. A slight drawback of REMPI, in comparison with, for instance, electron

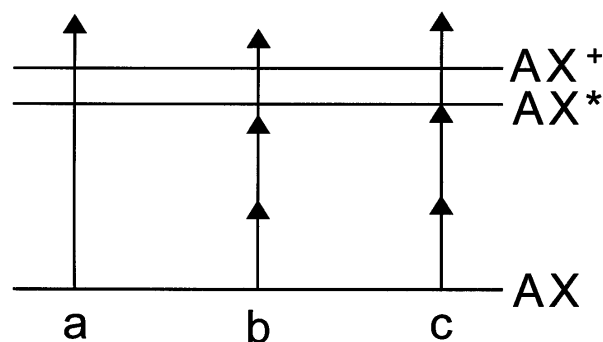


Figure 2. (a) Ionization via direct one-photon absorption, (b) non-resonant multi-photon ionization and (c) resonance enhanced multi-photon ionization (REMPI). Process (c) is an example of a (2 + 1) REMPI scheme; two photons are required to excite the molecule AX to a resonant excited intermediate state AX^* and one more to ionize AX^+ .

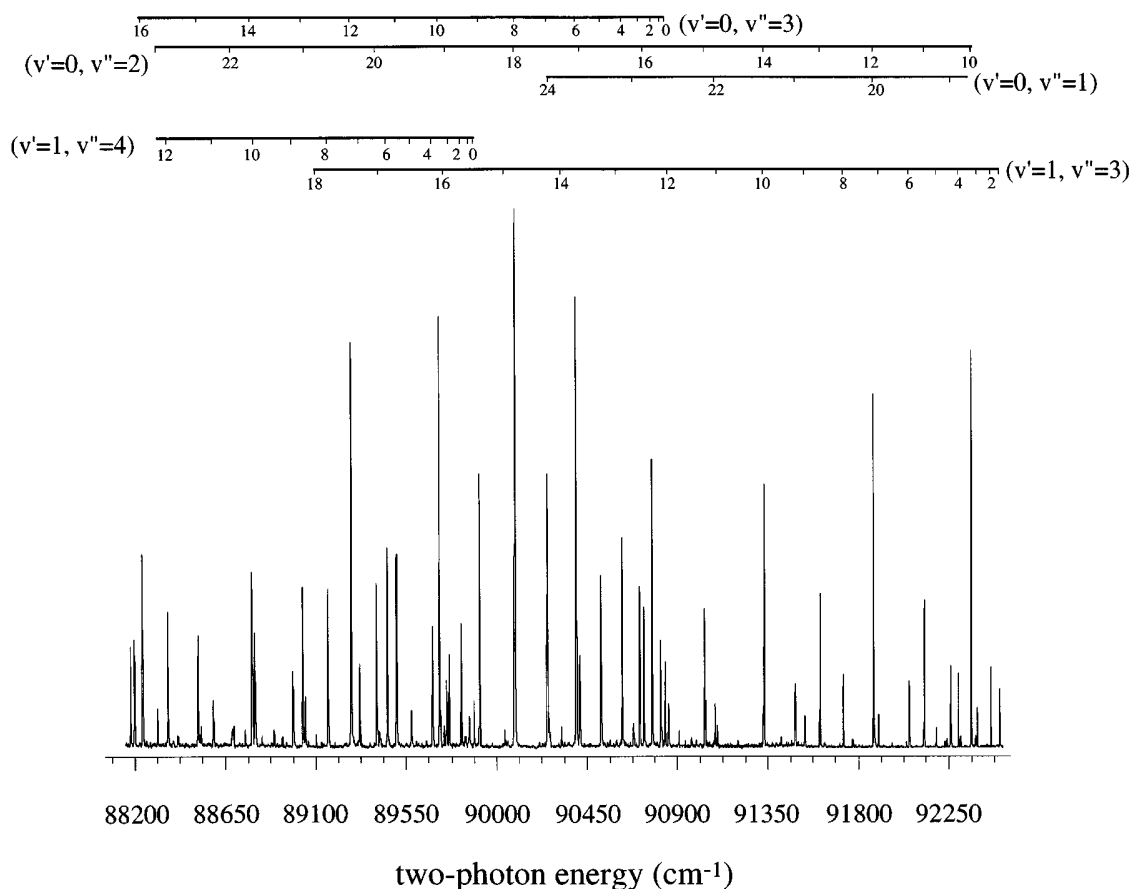


Figure 3. (2 + 1) REMPI spectrum of D_2 via the $E, F^1\Sigma_g^+$ ($v_E' = 0-1, J' = J''$) double minimum intermediate state showing the selective ionization of $D_2 X^1\Sigma_g^+$ ($v'' = 1-4, J''$) levels. D_2 molecules in various vibrational levels between $v'' = 0$ and $v'' = 4$ and rotational levels ranging from $J'' = 0$ to 26 were generated by the hot atom reaction $D + DI \rightarrow D_2 + I$ (adapted from Ref. 17).

impact ionization, is the requirement that the nature of the products and their spectroscopy be known, and the molecule must of course be optically active. At present many REMPI schemes have been characterized for a wide range of atoms, radicals and closed-shell molecules.^{18,19}

Photofragment time-of-flight mass spectrometry

In addition to the internal energy distributions, another observable of interest that can be measured following molecular photodissociation or a chemical reaction is the velocity (speed and angular) distribution of the products. Product velocities can be measured spectroscopically using Doppler spectroscopy.²⁰⁻²² A limitation of Doppler spectroscopy is that it is somewhat limited to fast-moving particles and thus relatively low-mass products (e.g. hydrogen atoms). Time-of-flight spectroscopy, measuring the distributions of times taken for particular fragments to traverse a well defined distance to a detector, in the absence of collisions, is a more common route to determine photofragment translational energy distributions.²³⁻²⁵ Time-of-flight distributions are usually measured through ionization of the reaction products using either electron impact ionization or REMPI, as ions are more conveniently detected than neutral molecules. Photofragment translational spectroscopy was pioneered by Wilson's group in the late 1960s. Over recent decades several tech-

nological improvements have been made and photofragment translational spectroscopy is now a generally applied method in uni- and bimolecular reaction dynamics.²²⁻²⁴ In the measurement of photofragment velocities we can distinguish two different observables, the speed (reflecting the kinetic energy release) and angular distributions.

Speed distributions. As mentioned above, following molecular photodissociation the nascent fragments start to recoil away from the point where they were 'born.' Measurement of speed distributions of photofragments will reveal directly the proportion of the excess energy that is deposited in the translational degrees of freedom. Through conservation of energy and momentum, the speeds of the two concomitant fragments are related to each other, and thus by measurement of the speed of one of the fragments we can obtain the total kinetic energy released into both fragments. If the photolysis energy is known (defined by the colour of the laser light) the translational energy distribution can also be used to determine the energy released into the other degrees of freedom, as

$$E_{\text{excess}} = E_{\text{photon}}(h\nu) - E_{\text{BDE}} \\ = E_{\text{translational}} + E_{\text{internal}}$$

An important parameter in time-of-flight measurements is the energy or velocity resolution, which is determined by experimental parameters. Detection of fine structure

in the translational energy distributions correlates directly with fine structure in the internal energy distribution. Energy resolution generally increases with increasing flight times, i.e. longer flight tubes. A new development in photofragment translational spectroscopy that has increased significantly the obtainable translational energy resolution is hydrogen Rydberg time-of-flight detection.^{22,26–28} In conventional translational energy spectroscopy, the photofragments are ionized close to where they are formed. Space-charge effects induced by high ion densities cause a decrease in the energy resolution. In Rydberg time-of-flight spectroscopy, photofragments are excited to very long-lived excited Rydberg states, which fly to the detector as neutrals, thus avoiding space-charge effects. Drawbacks of the Rydberg time-of-flight technique are that the technique has (largely) been applied to atomic hydrogen (or deuterium) fragments only, and it is less sensitive to slower moving particles. The translational energy resolution achieved by Rydberg time-of-flight spectroscopy is, however, unsurpassed. Ion imaging still requires the ionization of the photofragments, but with recent ion optical improvements (discussed below) the energy resolution achievable by ion imaging is ~ 50 meV at a kinetic energy of 1 eV.^{15,29}

Angular distributions. Photolysis products generally recoil in many directions from the point where they are generated. Photofragments which have the same speed but different angular directions will recoil as expanding spheres. When the dissociation is initiated by absorption of a linearly polarized photon the angular distribution of the photofragments is likely to be anisotropic, as the velocities of the fragments will be correlated with

the laser polarization vector. The polarization vector of the laser also defines a fixed frame in the laboratory. Angular recoil distributions depend on the direction of the laser polarization vector and the symmetries of the electronic states involved in the absorption process. To appreciate the source of this anisotropy we need to recall that absorption of light occurs through the coupling of the electric vector of the radiation, ϵ , and the transition dipole moment of a molecule, μ . For an ensemble of randomly rotating molecules the transition dipole moments μ have a random orientation with respect to the laser's electric field vector ϵ . The probability of absorption through an electric dipole-allowed excitation process is proportional to $|\mu\epsilon|^2$. Therefore, the laser will selectively interact with molecules which happen to be oriented such that their transition dipole moment lies parallel to ϵ . More generally we can say that $|\mu\epsilon| = |\mu| |\epsilon| \cos(\theta)$, where θ is the angle between the transition dipole moment and the electric field vector. Using linearly polarized light the probability of molecules absorbing photons will follow a $\cos^2(\theta)$ pattern. So far we have not considered the relationship between the transition dipole of the molecule, μ , and the molecular axis of the molecules. In simple bond cleavage processes fragments move apart by stretching an internuclear axis and, therefore, the relationship between the molecular axis and μ will determine in which direction the fragments recoil. We consider two limiting cases. Absorption through a parallel transition in which μ is directed parallel to the molecular axis is shown schematically in Fig. 4(a). Absorption via a perpendicular transition in which μ is directed perpendicular to the molecular axis is shown in Fig. 4(b). In case (a) the photofragments will primarily recoil along the

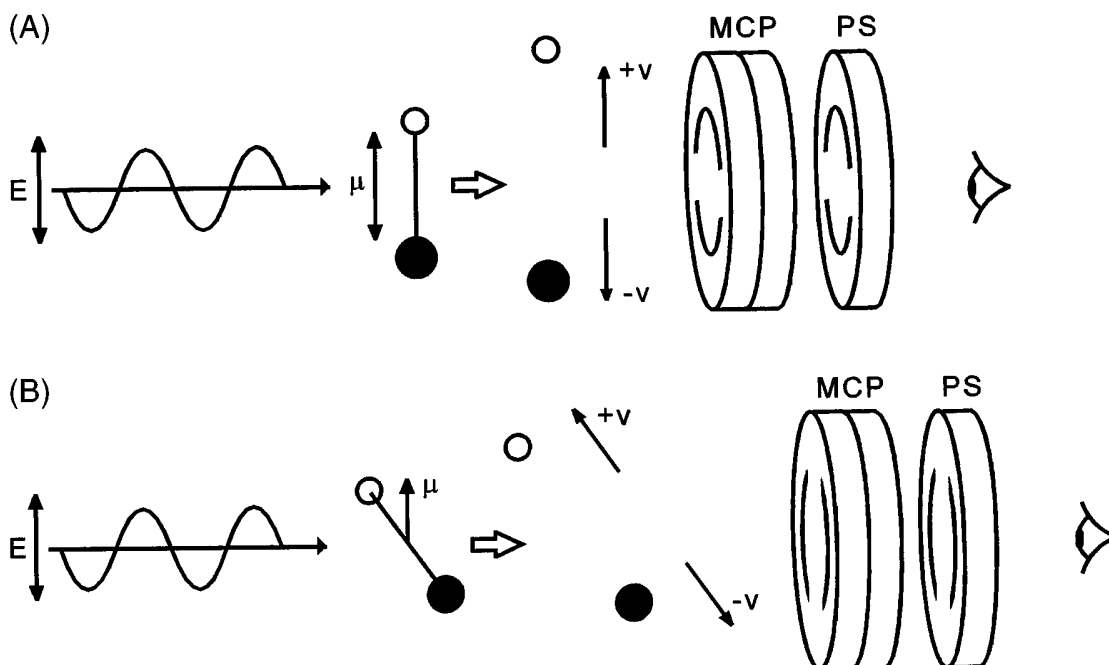


Figure 4. Photodissociation of a diatomic molecule via (a) a parallel and (b) a perpendicular transition. For parallel and perpendicular transitions the transition dipole moments, μ , lie parallel and perpendicular to the molecular axis, respectively. The photofragments recoil along the direction of the stretching molecular axis and, consequently, photofragments are produced parallel and perpendicular to μ . With the laser's polarization vector fixed in the laboratory frame, the photofragments will have anisotropic distributions. As described in more detail in the text, the speed and angular distributions are measured using a position-sensitive detector consisting of a pair of microchannel plates (MCP) coupled to a phosphor screen (PS).

laser polarization vector and in case (b) they fly away perpendicularly to the laser polarization vector.

More generally, the anisotropy function will have the form^{30,31}

$$I(\theta) = (4\pi)^{-1} [1 + \beta P_2(\cos \theta)]$$

where β has been termed the anisotropy parameter and P_2 is the second-order Legendre polynomial, $P_2(\cos \theta) = \frac{1}{2}(3 \cos^2(\theta) - 1)$. For the limiting cases, i.e. pure parallel or perpendicular transitions, β takes the values $+2$ and -1 , respectively. An isotropic angular distribution is characterized by $\beta = 0$, i.e. it is independent of angle θ . Product velocities are three-dimensional vector properties. The velocity distributions depend on the alignment between the transition dipole moment and the direction of the electric field. To measure the three-dimensional velocity distributions we ideally would like to have a three-dimensional spherical time-of-flight detector. Most time-of-flight devices are one-dimensional 'single point' detectors. As will be described in the subsequent section, ion imaging allows the measurement of the three-dimensional velocity distributions by measuring its two dimensional projection.

EXPERIMENTAL SET-UP

Figure 5 shows schematically the basic features of a conventional ion imaging apparatus. The photolyte (neat or seeded in a carrier gas) is expanded supersonically through a pulsed valve and introduced into the first stage of a differentially pumped vacuum chamber. The molecular beam is collimated by one or more skimmers before entering the reaction and detection regions, located in the second stage of the vacuum chamber. A few centimetres downstream the molecular beam passes through a hole in a repeller plate. Between the repeller and extractor plates the molecular beam is intersected by one or more linearly polarized laser beams. The usually short (~ 3 ns), and focused laser pulse provides a well defined starting point for the experiment in time

and space. Following photolysis the nascent fragments start to recoil. The products of interest are state-selectively ionized, usually by a second laser. Their expanding ion spheres are accelerated by an electric field towards the field-free time-of-flight tube. Typical fragment recoil speeds are around 1 km s^{-1} , which means that following a time-of-flight delay of $10 \mu\text{s}$ the spheres have expanded to measurable sizes. The flight times of the fragments, and thus the sizes of the images, can be adjusted experimentally by varying the magnitudes of the extraction fields in the time-of-flight region. At the end of this region the ions impinge upon a position-sensitive detector. The detector consists of a pair of chevron-type microchannel plates (MCP) coupled to a fast phosphor screen. The reader interested in these and alternative position sensitive detectors is referred to recent feature articles on focal plane detectors.^{32,33} In order to detect ions mass selectively, the front plate of the microchannel plate detector is briefly pulsed to a negative voltage upon arrival of the ions of interest, thus ensuring maximum gain through the detector. The ions generate an electron signal on the MCP channel on which they impinge. These electron signals are amplified through the MCP assembly and induce phosphorescence on the phosphor screen. The phosphorescence is coupled out of the vacuum chamber via a fibre-optic bundle. Two-dimensional time-of-flight profiles are recorded by imaging the output of the fibre-optic bundle onto a charge-coupled-device (CCD) camera.

Using the experimental set-up shown in Fig. 5, information on the coordinate of the recoil velocity parallel to the propagation direction of the molecular beam is 'lost,' but the two velocity components perpendicular to the molecular beam propagation are directly measured on the detector. More quantitative information is obtained from the images when the full three-dimensional velocity distributions can be reconstructed from the crushed two-dimensional time-of-flight profiles. In ion imaging, the initial three-dimensional distributions of the photofragments are projected on to the face of a two-dimensional position sensitive detector. As

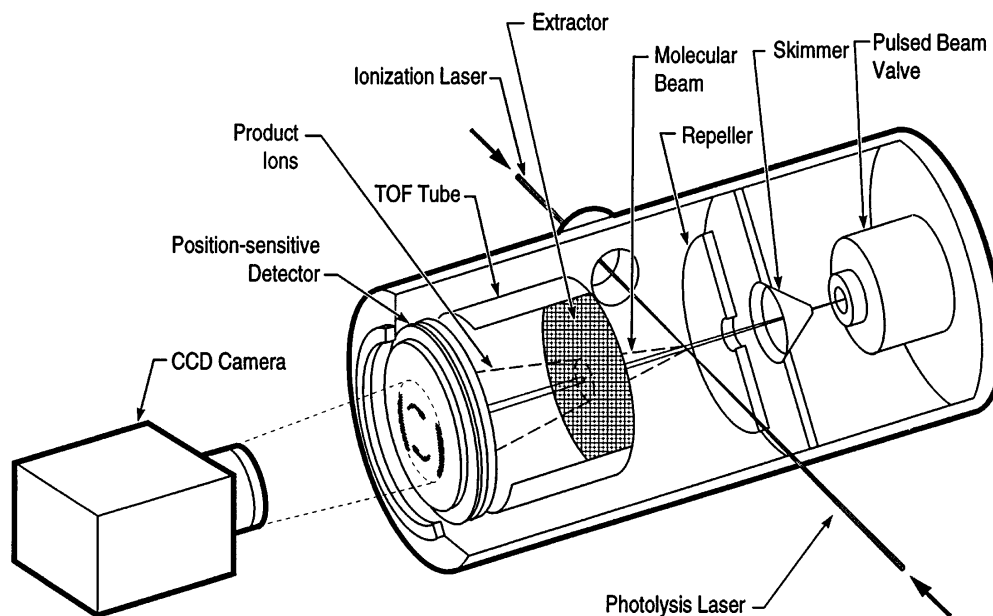


Figure 5. Schematic diagram of a photofragment imaging apparatus.

long as the face of the detector is parallel to the photolysis laser polarization vector, the initial three-dimensional product distributions can be reconstructed from these two-dimensional projections using a direct mathematical transformation, i.e. the inverse Abel transformation.^{3,34} Figure 6 shows the kind of images that may be recorded for a hypothetical photolysis producing fragments of a single speed. The position where the molecular beam hits the plane of the detector, which is in a good approximation also the position of the centre of mass of the molecule, is indicated by a cross. On the left of Fig. 6 a simulated image is shown for a pure perpendicular transition ($\beta = -1$). The photofragments recoil primarily perpendicular to the laser polarization vector (its direction is indicated by the black arrow on the right of Fig. 6), which is also an axis of cylindrical symmetry for the three-dimensional distributions. A perpendicular transition produces a ring of photofragments around the 'equator' of a sphere. In the two-dimensional crushed image the ion density will be highest at the outer ends of the rings, but there will also be photofragments hitting the detector more to the centre of the image. The corresponding inverse Abel transformed reconstructed images are generally (and here) displayed by taking a slice through the full three-dimensional distribution. The full three-dimensional dis-

tribution is then obtained by rotating this slice around the laser polarization vector (i.e. the axis of symmetrical symmetry). On the right of Fig. 6 the image is shown obtained following a parallel transition. Photofragments recoil primarily parallel to ϵ displaying a $\cos^2(\theta)$ angular distribution ($\beta = 2$). The two-dimensional crushed image shows fragments at the poles of the crushed spheres. In the middle column images are shown measured in the case when the fragments have an isotropic angular distribution. The sort of information that may be obtained from the images is best described using a few experimental examples. First, the principal capabilities of the ion imaging technique will be highlighted using results on the UV photolysis of a diatomic molecule, deuterium iodide (DI).

Before we continue, it might be relevant to point out the differences between ion imaging and closely related, so-called, coincidence techniques, which are often used to study gas-phase reaction dynamics of species propagating in a fast ion or neutral beam.^{32,35-39} Ion imaging relies on the fact that when a photodissociation event occurs to give two fragments, their dynamics are constrained by conservation of energy and momentum. Measuring the position and speed of *one* 'known' fragment is all that is necessary to determine the position and speed of the concomitant fragment. If one cannot

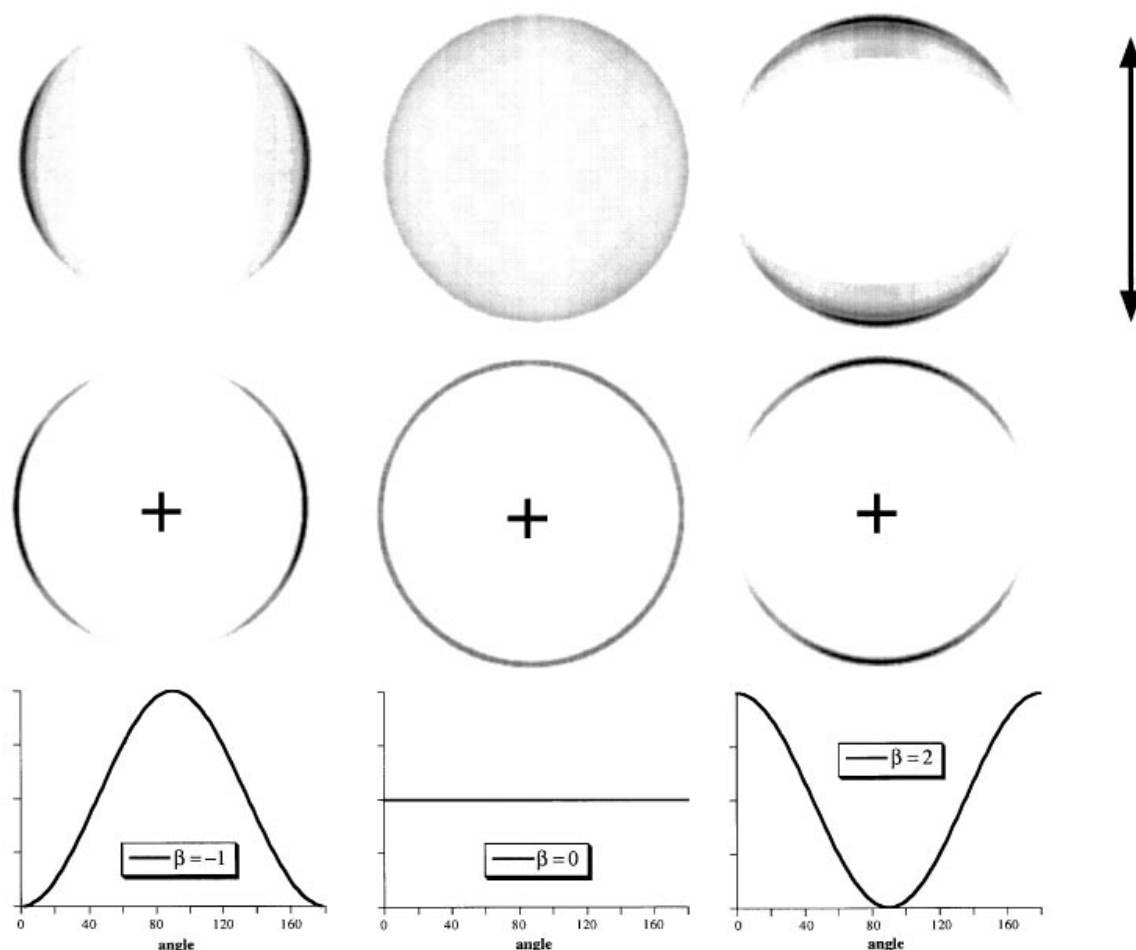


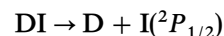
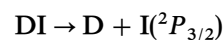
Figure 6. The top row shows simulated two-dimensional images corresponding to anisotropy parameters $\beta = -1, 0$ and $+2$ (see text). The arrow indicates the direction of the laser field's polarization. In the middle row the intensity distributions of the photofragments through the centre of the image are shown derived from the inverse Abel transformed images. Rotation of these slices around the laser polarization vector provide the full three-dimensional photofragment distributions.

determine the identity of the fragment, as may be the case for dissociations producing fast neutrals, the velocity of both fragments must be determined in correlated pairs. Coincident techniques measure these pair correlations. A fundamental difference between coincident techniques and the ion imaging technique is that with coincidence techniques all internal state information must be obtained by velocity resolution in a manner similar to conventional time-of-flight methods. Generally, in coincidence studies no spectroscopic means are used to provide state selectivity in fragment detection. However, if the correlated velocity information is of sufficient resolution, similar dynamic processes can be studied with coincidence techniques to those with the ion imaging technique.

DI photolysis

Photodissociation of a diatomic molecule is a simpler process than the photolysis of a polyatomic molecule as the two fragments formed in the photolysis of a diatomic cannot possess vibrational or rotational energy. The photodissociation of HI/DI using UV radiation has been widely studied, both experimentally^{40–44} and theoretically.^{45,46} It is an important reaction as it is often used as a source of 'hot' hydrogen/deuterium atoms in the study of bimolecular reactions. The pho-

tolysis of hydrogen iodide involves complex dynamics as more than one electronic excited state contributes to the UV absorption spectrum. The UV absorption continuum of hydrogen iodide, a broad, featureless absorption peaking around 220 nm, arises from at least three and probably four different electronic excited states.⁴⁵ Transitions to these states arise from two parallel- and two perpendicular-type electronic transitions. The least energetic parallel transition is a $^3\Pi_0^+ \leftarrow ^1\Sigma^+$ transition, and the two perpendicular transitions are $^3\Pi_1 \leftarrow ^1\Sigma^+$ and $^1\Pi_1 \leftarrow ^1\Sigma^+$. A fourth repulsive state in the first absorption continuum, the $^3\Sigma_1^+$ state, was previously assumed to be too high in energy to contribute any parallel character to the dissociation process. The electronic states involved in the UV photolysis of hydrogen iodide are shown schematically in Fig. 7. Early molecular beam time-of-flight studies on the photodissociation of DI revealed that two product channels exist:



where $\text{I}(^2P_{3/2})$, or I, is the ground state iodine and $\text{I}(^2P_{1/2})$, or I^* , is the excited spin orbit state of iodine ~ 0.9 eV in energy above the ground state. Early experimental work focused on measuring the branching ratios, the broad continuous absorption spectrum could

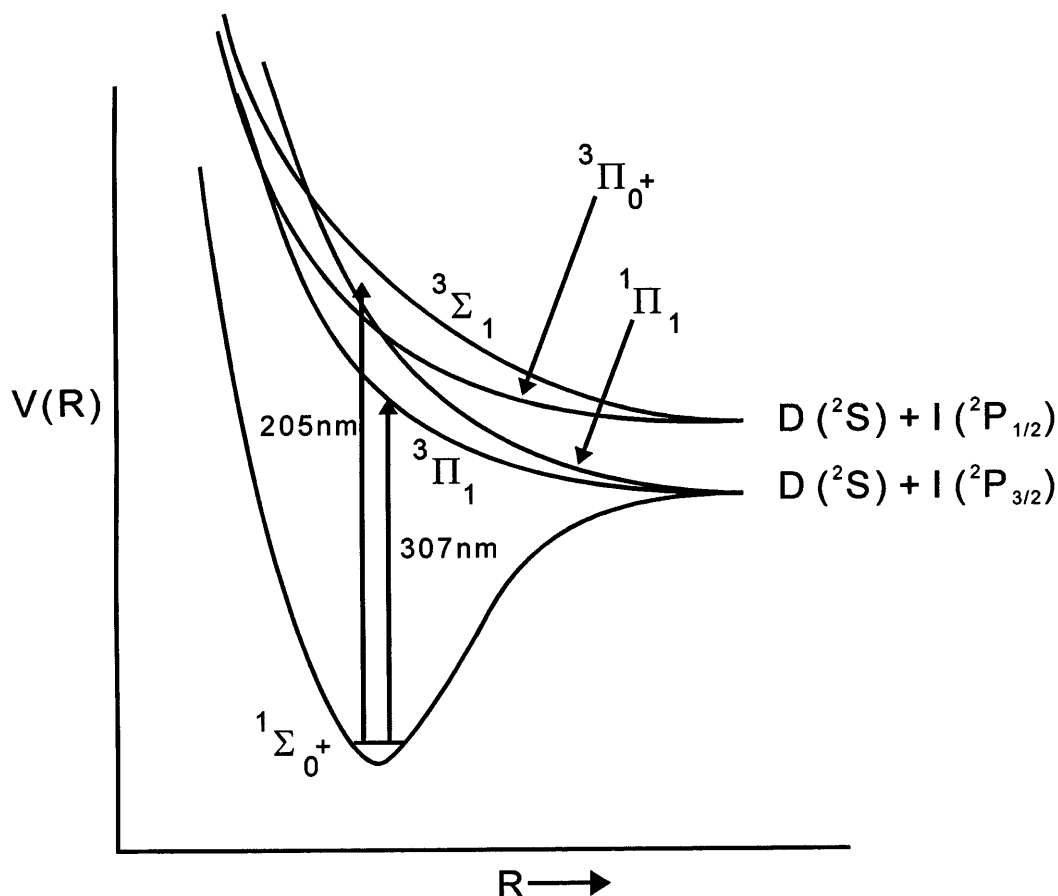


Figure 7. Schematic diagram of the potential energy curves involved in the UV photolysis of DI. The excited states $^3\Pi_1$ and $^1\Pi_1$ converge to ground-state iodine atoms, I or $\text{I}(^2P_{3/2})$, whereas the $^3\Sigma_1$ and $^3\Pi_0^+$ excited states lead to spin-orbit excited state iodine atoms, I^* or $\text{I}(^2P_{1/2})$. The I/I^* branching ratio depends on the relative contribution of each of these excited states to the absorption process. Transitions to the excited states forming ground-state I atoms are perpendicular in character, whereas those forming excited I^* atoms are parallel, as reflected in the ion images.

be deconvoluted into its various components. Already in 1975 Wilson and co-workers⁴¹ provided the first experimental evidence that both parallel- and perpendicular-type dissociation channels are active in the UV DI photolysis. Subsequent studies by Schmiedl *et al.*⁴² and van Veen *et al.*⁴³ allowed the qualitative experimental determination of the variation in the I*/I branching ratio as a function of energy. One of the most comprehensive theoretical investigations of the photodissociation dynamics of HI and DI has been reported by Levy and Shapiro.⁴⁶ These authors generated non-adiabatic potential energy curves for the first four excited electronic states of HI and DI, I*/I product branching ratios as a function of dissociation wavelength and anisotropy parameters describing the dissociation dynamics. These theoretical predictions are found to be in general agreement with the available

experimental data. However, some discrepancies between the theoretical predictions and subsequent experimental ion imaging data have been found.

Knowing the energy of the photolysis photon and the D—I bond dissociation energy (BDE = 3.05 eV or 24955 cm⁻¹), the speed of the nascent D atoms can be calculated. Two D atom translational energies are anticipated corresponding to the two different spin orbit states of the accompanying iodine atom. Assuming that the parent DI has negligible internal energy, the nascent D atoms will have a kinetic energy corresponding to

$$E_{\text{trans}}(\text{D}) = E_{(h\nu)} - \text{BDE} - E_{\text{trans}}(\text{I}) - E_{\text{internal}}(\text{I})$$

Figure 8 shows a series of ion images of nascent D atoms obtained at three different photolysis energies. In these experiments, a single laser beam was employed both to dissociate the DI and to ionize the resulting D

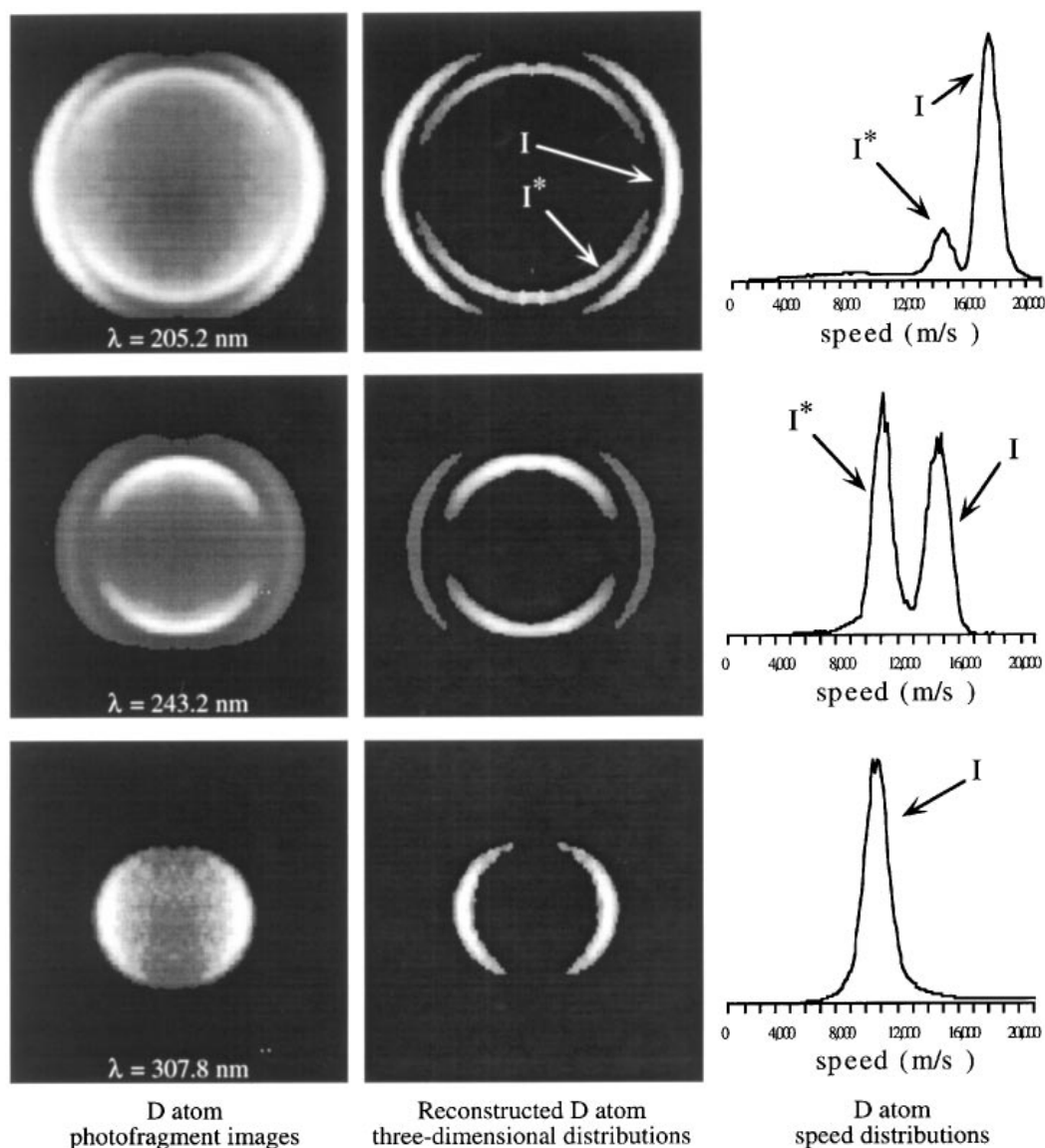


Figure 8. Images of D atoms produced in the UV photolysis of DI. The top row shows, from left to right, the two-dimensional image, the inverse Abel transformed image and the speed distribution of D atoms formed in the 205.2 nm photolysis of DI. The image shows two distinct features, an outer $\sin^2(\theta)$ ring (reflecting a perpendicular transition) corresponding to the production of faster D atoms, formed concomitantly with ground-state iodine atoms and an inner $\cos^2(\theta)$ ring (reflecting a parallel transition) corresponding to the production of slower D atoms, formed concomitantly with spin-orbit excited iodine. The middle and bottom rows show the data obtained at photolysis laser wavelengths of 243.2 and 307.8 nm, respectively.

atoms using either (3 + 1) or (2 + 1) REMPI schemes. At 205.2 nm (6.04 eV), the photolysis produces two distinct rings observable in the raw data and in the Abel transformed images. The outer ring corresponds to the production of ground-state iodine and the inner ring to the production of excited-state iodine. At 307.8 nm, the D-atom ionization occurs via (3 + 1) REMPI through the D ($n = 3$) intermediate state. The ionization laser frequency is one third that of the D-atom Lyman- β transition frequency, i.e. 307.8 nm. This photon energy is close to the threshold for D + I* formation, a channel not observed in this ion image. At 243.2 nm (5.10 eV), the D-atom ionization occurs via (2 + 1) REMPI through the D ($n = 2$) intermediate state. The ionization laser frequency is half that of the D-atom Lyman- α transition frequency.

What information is inherent in the images in Fig. 8? From the measurement of the size of the rings and the arrival time of the ions at the detector, the speed of the D atoms is easily determined. This can best be done using the inverse Abel transformed images. From this measurement and the knowledge of the photolysis energy, the bond dissociation energy may be determined. Our three measurements give an average bond dissociation energy of 3.05 eV. From analysis of the inverse Abel transformed data we can determine both the branching ratios for dissociation and the angular distribution of the two channels, described by the anisotropy parameter β . Inverse Abel transformed images are shown in the middle column of Fig. 8. Resulting D atom speed distributions obtained from integration over, and appropriate weighting of, the data in the inverse Abel transformed images are shown on the right part of Fig. 8. As can be seen from the images, the branching ratios between the I and I* channels change dramatically with photolysis energy. At low energy only the I channel is observed and a single ring is seen that has a pure $\sin^2(\theta)$ angular distribution. As the energy is increased, the I* channel becomes energetically accessible and an additional component, having a $\cos^2(\theta)$ distribution, is seen in the images. An I*/I branching ratio of 1.25 is observed at a 243.2 nm photolysis wavelength. This can be compared with the calculated values of 1.25 by van Veen *et al.*⁴³ or 1.4 by Levy and Shapiro⁴⁶ or an experimental value of 1.5 measured⁴⁰ at 240 nm. At a 205.2 nm photolysis wavelength the I*/I branching ratio has become 0.25 and calculations predict 0.25.^{43,46} The images are a velocity representation and not an energy projection of the fragments, and therefore the rings appear closer together relative to the size of the image at the 205.2 nm than at the 243.2 nm photolysis wavelength. Interestingly, the calculations of Levy and Shapiro⁴⁶ predict a significant change in the anisotropy parameter for the I* channel, changing from $\beta = 1.0$ at 243.2 nm to -0.3 at 205.2 nm. In contrast, our images reveal that the anisotropy parameter β is ~ 2 at both photolysis wavelengths, corresponding to exclusive parallel character of the transitions.

CD₃I photolysis

In contrast to the photolysis of a diatomic molecule, the products formed in the photolysis of a polyatomic mol-

ecule can be molecular, and hence possess vibrational and rotational degrees of freedom. To illustrate how this alters matters, we look at the 'polyatomic analogue' of DI, CD₃I. Methyl iodide and its perdeuterated analogue are benchmark molecules in polyatomic molecular photodissociation studies. The photolysis of methyl iodide has been studied by a wide range of spectroscopic and time-of-flight techniques.⁴⁷⁻⁵⁰ It was also the first molecular photodissociation used to demonstrate the abilities of the ion imaging method.¹ Photofragmentation of methyl iodide using $\lambda = 266$ nm radiation (i.e. the fourth harmonic of a YAG laser) produces predominantly methyl radicals and atomic iodine atoms:



As for hydrogen iodide, the iodine atom can be formed in its electronic ground or spin-orbit excited states. The concomitant methyl fragments can be formed with kinetic, and now also internal energy. The internal energy may be deposited in vibrational and rotational degrees of freedom. An important question to ask is whether and how the I/I* branching ratio correlates with the quantum state of the concomitant methyl radical formed in the dissociation. Additionally, it is interesting to probe which vibrational and rotational modes of the methyl radicals are excited. It is known that the UV absorption around 266 nm involves a mostly parallel transition and therefore, it is anticipated that the C_3 symmetry axis will be preserved. Therefore, the number of vibrational modes of the methyl fragments that will be excited is restricted to just two, the symmetric stretch, ν_1 , and the umbrella mode, ν_2 . Methyl iodide is a symmetric top molecule and methyl radicals are in their ground state planar. Therefore, one can hypothesize that the umbrella mode, ν_2 , of the methyl will be excited following the photolysis. To measure the correlated quantities (I/I* ratios correlated to the amount of rotational and vibrational excitation of the CD₃ fragments), ion images were recorded for state-selectively ionized methyl fragments.⁵¹ An experimental problem is that REMPI spectra of methyl radicals, using the $3p_z \ ^2A_2''$ resonant intermediate state are perturbed as the intermediate state is predissociative.⁵² The rate of predissociation of the analogous state of CD₃ is slower and, therefore, many experimental studies have actually focused on CD₃I instead of CH₃I. REMPI data have revealed that nascent CD₃ fragments are predominantly formed with vibrational excitation of the ν_2 umbrella mode, although some minor excitation of the ν_1 stretching mode was detected.^{51,52} Figure 9 shows the (2 + 1) REMPI spectrum of the 0_0^0 band of CD₃ (probing methyl fragments with $\nu_2 = 0$) formed via $\lambda = 266$ nm photolysis of CD₃I. Other REMPI transitions were used to probe methyl fragments with different amount of excitation in ν_2 .⁵¹ The recorded images showed, just like the D images in Fig. 8, two rings corresponding to the formation of I and I*. The CD₃ angular distributions could be described by anisotropy parameters β of ~ 2 , for both rings, revealing that these CD₃ photofragments are formed via a prompt dissociation following photoabsorption through a parallel transition. The I/I* ratio was found to change dramatically with increasing ν_2 vibrational excitation of the methyl fragment. It was found that the I/I* ratios were

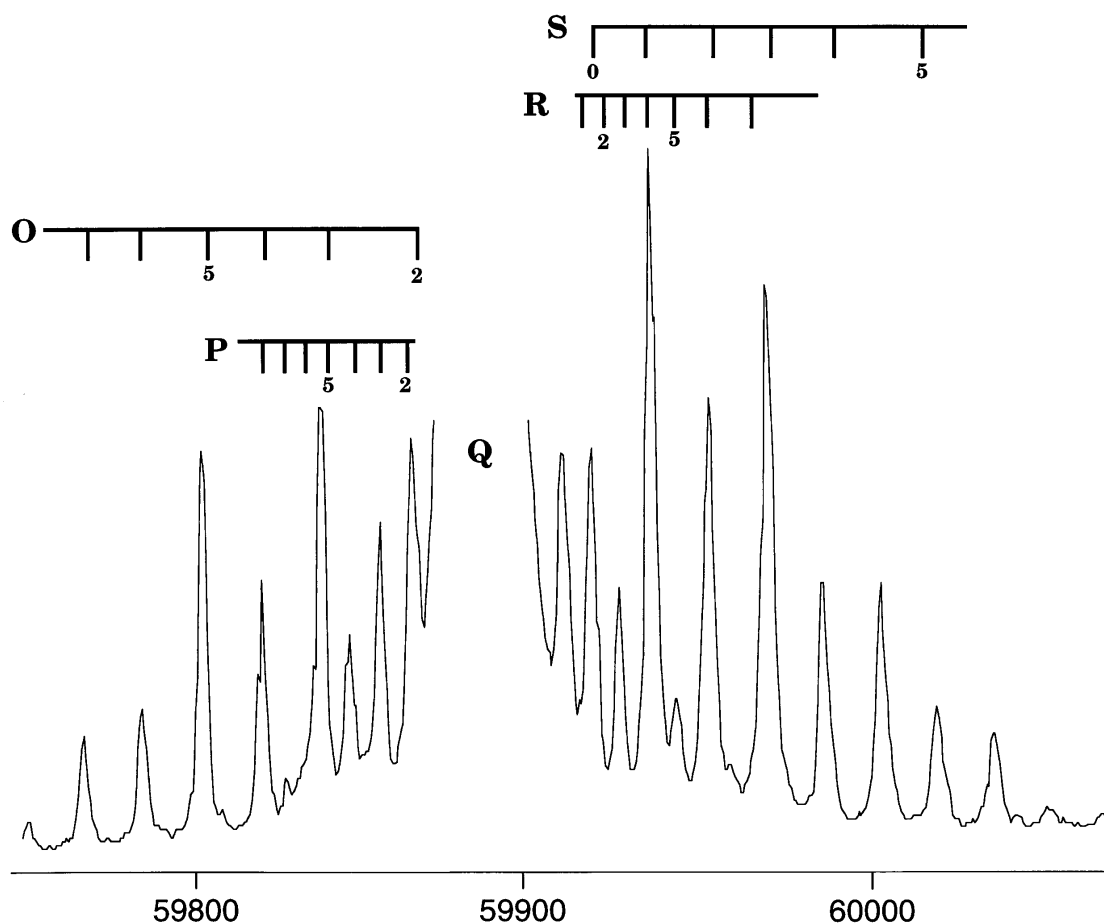


Figure 9. (2 + 1) REMPI spectrum of CD_3 photofragments, formed via the $\lambda = 266$ nm photolysis of CD_3I , ionized through the $3p_z \times 0_0^0$ band. The spectrum shows the different rotational states populated in the CD_3 fragment in $v_2 = 0$. The intense band in the middle represents the Q -branch. Similarly, CD_3 photofragments with various numbers of vibrational quanta in v_2 can be ionized and 'ion imaged' separately (data not shown). Adapted from Ref. 51.

0.04, 0.09, 0.27 and 1.4 for v_2 in $v = 0, 1, 2$ and 3, respectively. These results were explained by variations in curve-crossing probability depending on the velocities of the fragments at the curve-crossing point (Landau-Zener effect).

In general, polyatomic molecular photodissociation can produce a wide range of reaction products. In several cases, notably the photolysis of ozone,⁵³ the VUV photolysis of methane^{54,55} and the UV photolysis of HNCO ,^{56,57} ion imaging has contributed significantly in unravelling product branching ratios, quantum state populations and the understanding of the underlying reaction dynamics.

Imaging of state-selected, oriented CD_3I molecules

Using ion imaging, quantum-state selectivity in *product* detection is readily achieved; however, quantum-state selectivity in *precursor* selection is more difficult and requires additional efforts. Supersonic molecular beams produce generally 'cold' precursor molecules with most of the population in the electronic and vibrational ground levels. Although molecules in a molecular beam are also cooled rotationally, the rotational population is usually still spread over a range of lower rotational

levels. Normally all these different rotational levels will be excited simultaneously. Clearly an experiment that starts with only a single quantum state and measures the same information about the photofragments would lead to an even more direct view of the dissociation dynamics.

A hexapole device can be used to select a single rotational state and thus provide a source of state-selected precursor molecules.⁵⁸ Symmetric top molecules, such as methyl iodide, travel through the electric field of a hexapole following sinusoidal trajectories. Different rotational states are focused at different points depending on the strength of the hexapole field. Placement of a small pinhole at the end of the hexapole allows the selective transmission of molecules in a particular rotational (denoted by the quantum numbers JKM) state. An additional advantage of using a hexapole state selector is that focusing will typically lead to an increased density in the molecular beam. The combination of rotational state selection and photofragment imaging was introduced by Janssen and co-workers.^{59,60} Even more control was accomplished by the same group by spatially orienting the precursor molecules, achieved by applying an electric field across the molecular beam. Their first application of the combination of hexapole state selection, orienting the precursor molecule, and ion imaging was on perdeuteromethyl iodide.

As in the case of non-oriented, non-state-selected molecules^{51,52,61} (see also Fig. 9), rotational distributions of the methyl fragments in $v_2 = 0$ were probed using REMPI, but now for rotational state-selected precursor molecules.^{60,62} An interesting observation was made in that the rotational state-selected precursor CD_3I molecules tend to preserve the quantum number K from the precursor to the CD_3 fragments. Additionally, images were recorded for the I^* photofragments. Figure 10 shows three 'raw' ion images of nascent I^* fragments formed in the $\lambda = 266$ nm photolysis of $JKM = 111$ state-selected CD_3I molecules. The I^* fragments were ionized by a second laser beam. The difference in the three images stems from the differences in the field strength used to orient the rotational state-selected molecules. In the upper image no field was employed, for the middle image an orienting field of ~ 100 V cm^{-1} was used, whereas for the third image a field of 1600 V cm^{-1} was employed. The orientation of the field was directed along the photolysis laser polarization vector. It is immediately clear that the CD_3I molecules have been oriented by the electric field as the last image shows that the I^* atoms primarily recoil in only one direction. For non-oriented CD_3I molecules the recoil of the I^* fragments following 266 nm photolysis of $JKM = 111$ state-selected CD_3I could be described by an anisotropy parameter β of ~ 2 . Similar measurements on state-selected $JKM = 212$ precursor molecules demonstrated that the on-axis density distribution of oriented CD_3I molecules depends not only on the magnitude of the field (as revealed by the images in Fig. 10), but also on the nature of the individual selected JKM states, as predicted by theory. It was predicted and measured that a 'full strength' orientating field produces a distribution of $JKM = 212$ CD_3I molecules with a small node at $\theta = 0$, i.e. directly along the direction of the orienting field.⁶⁰

Velocity mapping

To obtain true three-dimensional distributions from the images, the products' velocity components perpendicular to the molecular beam direction have to remain unchanged by the extraction fields. In the initial design, the holes in the extractor plates were covered by grids to ensure that the extraction field lines were parallel to the molecular beam direction. However, parallel fields also project the whole interaction volume (defined by the intersection of the laser and molecular beam) on to the detector, which may lead to a significant blurring of the image. The grids may cause further distortions by deflecting the ions. For an interesting, related discussion on the effects of lenses and penetrating fields in time-of-flight mass spectrometry, the reader is referred to a recent feature article in this journal by Guilhaus.⁶³ Recently, Eppink and co-workers^{15,29,64} introduced to ion imaging an ion optical modification, removing the grids and employing a set of electrostatic lenses around the reaction region. The electrostatic lenses make it possible to focus ions possessing the same initial velocity on to a single point (pixel) on the position sensitive detector. 'Velocity mapping,' as this modification was termed by Eppink and co-workers, greatly increases the achievable velocity (and thus kinetic energy) resolution.

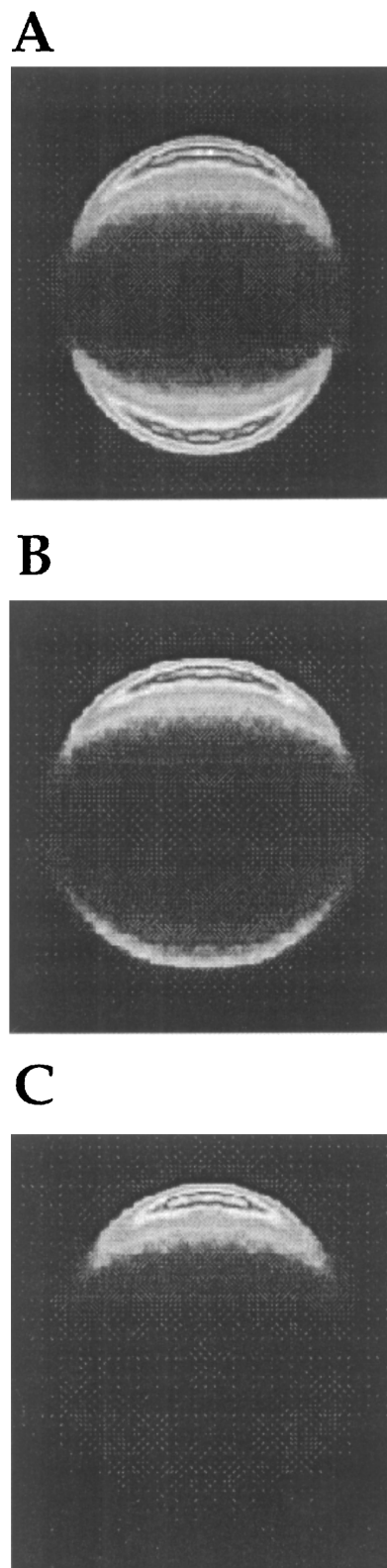


Figure 10. Ion images of I^* fragments generated via the $\lambda = 266$ nm photolysis of state-selected and oriented (JKM) = (111) CD_3I molecules. The orientation field was parallel to the plane of the detector and the linear polarization of the dissociation laser. The electric field orients the CD_3I molecules with the iodine-end pointing upwards. The orientation field strength increases from 0 V cm^{-1} for image A, 96 V cm^{-1} for B and 1600 V cm^{-1} for image C. As can be seen, the proportion of I^* recoiling upwards increases as the orientation field strength increases, reflecting the increased degree of orientation of the methyl iodide molecules. Adapted from Ref. 60.

Parker and Eppink¹⁵ demonstrated the improved capabilities of the modified ion imaging apparatus by investigating the complex competing pathways possible in the photoionization and dissociation of molecular oxygen excited to the $v = 2, N = 2$ level of the $3dp\ ^3\Sigma_{1g}^-$ Rydberg state. By absorbing a subsequent photon, these excited intermediate states may (i) dissociate, generating ground- and excited-state oxygen atoms (the latter being ionized by a subsequent photon), (ii) autoionize, forming O_2^+ ions in ground or excited states, (iii) autoionize and dissociate, forming O^+ and ground- and excited-state O atoms, or (iv) autoionize and dissociate after absorption of one or more photons. In total, more than 10 different channels are expected, which normally would hamper any sort of analysis.

An interesting characteristic of ion imaging instruments is that they may be converted, without major modifications, into photoelectron imaging instruments.¹³ Owing to the enhanced velocity resolution and by combining results of the O^+ images with the images of the corresponding photoelectrons, Parker and Eppink were able to unravel the relative importance of most of the anticipated channels, all exhibiting different kinetic energy releases and different angular recoil. Figure 11 shows on the left the ion image of the O^+ ions and on the right the corresponding image of the photoelectrons. The positions of the rings corresponding to the formation of O^* atoms are indicated, and also the positions of the rings involving intermediate $O_2^+(v)$ states. Channels separated by less than 100 meV in kinetic energy are still well resolved. This improvement, brought about by a relatively simple modification, increases the resolution in the images tremendously and is expected to enhance the capabilities of photofragment ion imaging even more.

CONCLUSION

The study of unimolecular dissociations of gas-phase molecules is of great importance in the characterization of potential energy surfaces and the resulting intramolecular forces which govern the dynamics. If we wish to exert more control over chemical reactions, including steering the particular products produced, we will need to understand in detail the making and breaking of chemical bonds at the molecular level. The ion imaging technique, with its combination of position-sensitive detectors based on microchannel plate and fibre-optical technology, along with state-selective detection using optical spectroscopy, has made possible the detailed study of many uni- and bimolecular reactions, unravelling often complex reaction dynamics. In principle, the resolution of the velocity measurement is limited by the resolution of the microchannel plate detectors (about 50 μm) and the number of pixels on the CCD array. In order to reach these limits there are several experimental parameters that have to be accounted for. The quantum-state selectivity will always be dictated by the spectroscopy of the molecule. The recently introduced 'velocity mapping' technique has greatly diminished the importance of the size of the interaction volume and the molecular beam velocity spread, which used to have a negative effect on the achievable energy resolution in the conventional imaging set-up.

We described the alignment, observed in the images, between the velocity of photofragments and the transition dipole moment ($\mu-v$ correlation), but other alignment effects can also be observed by ion imaging, such as the alignment between the velocity of the photofragments and their rotational angular momentum ($v-J$

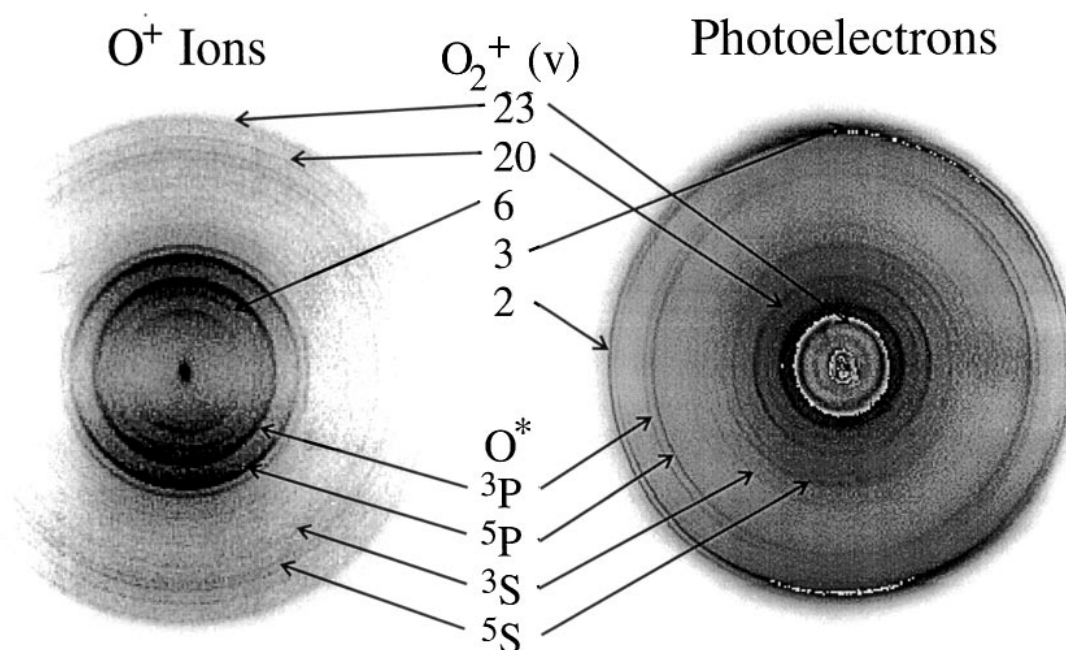


Figure 11. Photolysis and ionization of O_2 through the $v = 2, N = 2$ level of the $3dp\ ^3\Sigma_{1g}^-$ Rydberg intermediate state. On the left a raw O^+ ion image is shown, on the right the corresponding 'raw' photoelectron image. Particularly appealing features of these 'velocity mapping' images are the vast number of extremely sharp rings observed in both the photoelectron and photofragment images. Rings that correspond to O_2^+ vibrational levels and excited O^* atoms are indicated in both images. The laser polarization vector was vertical for both these images. Intensities are shown in a linear grey scale (darker corresponds to higher intensities). Reproduced from Ref. 15.

correlation),⁶⁵ or the alignment between an atom's velocity and its orbital angular momentum.^{64,66,67} Ion imaging has also been used to investigate the effects of high electric laser fields on photodissociation and ionization.⁶⁸

In the 10 years that ion imaging has been applied to study gas-phase reaction dynamics it has contributed significantly to our understanding of the dynamic forces which govern the breaking and making of chemical bonds, even when the reactions under study are complex, producing many different products with populations spread over an array of quantum states. An

attractive aspect of ion imaging is the simultaneous measurement of a range of quantities important in photodissociations and bimolecular reactions.

Acknowledgements

We acknowledge the following workers for providing material used in the work described in this paper: David Neyer and David Chandler, Sandia National Laboratories, Livermore (USA), Maurice Janssen and Steven Stolte, Vrije Universiteit Amsterdam (The Netherlands) and Andre Eppink and David Parker, Katholieke Universiteit Nijmegen (The Netherlands).

REFERENCES

- D. W. Chandler and P. L. Houston, *J. Chem. Phys.* **87**, 1445 (1987).
- B. J. Whitaker, in *Research in Chemical Kinetics*, edited by R. G. Crompton and G. Hancock, Vol. 1, pp. 307–345. Elsevier, Amsterdam (1993).
- A. J. R. Heck and D. W. Chandler, *Annu. Rev. Phys. Chem.* **46**, 335 (1995).
- P. L. Houston, *Acc. Chem. Res.* **28**, 453 (1995).
- P. L. Houston, *J. Phys. Chem.* **100**, 12757 (1996).
- A. J. R. Heck, *Eur. Mass Spectrom.* **3**, 171 (1997).
- M. A. Buntine, D. P. Baldwin, R. N. Zare and D. W. Chandler, *J. Chem. Phys.*, **94**, 4672 (1991).
- T. N. Kitsopoulos, M. A. Buntine, D. P. Baldwin, R. N. Zare and D. W. Chandler, *Science* **260**, 1605 (1993).
- T. N. Kitsopoulos, M. A. Buntine, D. P. Baldwin, R. N. Zare and D. W. Chandler, *SPIE* **1858**, 2 (1993).
- A. G. Suits, L. S. Bontuyan, P. L. Houston and B. J. Whitaker, *J. Chem. Phys.* **96**, 8618 (1992).
- L. S. Bontuyan, A. G. Suits, P. L. Houston and B. J. Whitaker, *J. Phys. Chem.* **97**, 6342 (1993).
- D. W. Chandler, T. N. Kitsopoulos, M. A. Buntine, D. P. Baldwin, R. I. McKay, A. J. R. Heck and R. N. Zare, in *Springer Series in Chemical Physics*, edited by J. Wolfrum, H.-R. Volpp, R. Rannacher and J. Warnatz, Vol. 61, pp. 42–66. Springer, Heidelberg (1966).
- H. Helm, N. Bjerre, M. J. Dyer, D. L. Huestis and M. Saeed, *Phys. Rev. Lett.* **70**, 3221 (1993).
- M. Saeed, M. J. Dyer and H. Helm, *Phys. Rev. A* **49**, 1491 (1994).
- D. H. Parker and A. T. J. B. Eppink, *J. Chem. Phys.* **107**, 2357 (1997).
- M. N. R. Ashfold and J. D. Howe, *Annu. Rev. Phys. Chem.* **45**, 57 (1994).
- A. J. R. Heck, W. M. Huo, R. N. Zare and D. W. Chandler, *J. Mol. Spectrosc.* **173**, 452 (1995).
- S. L. Anderson, *Adv. Chem. Phys.* **82**, 177 (1992).
- M. N. R. Ashfold, S. G. Clement, J. D. Howe and C. M. Western, *J. Chem. Soc., Faraday Trans.* **89**, 1153 (1993).
- M. P. Docker, A. Hodgson and J. P. Simons, in *Molecular Photodissociation Dynamics*, edited by M. N. R. Ashfold and J. E. Baggot, Vol. 1, pp. 115–137. Royal Society of Chemistry, London (1987).
- Z. Xu, B. Koplitz and C. Wittig, *J. Chem. Phys.* **87**, 1062 (1987).
- M. N. R. Ashfold, I. R. Lambert, D. H. Mordaunt, G. P. Morley and C. M. Western, *J. Phys. Chem.* **96**, 2938 (1992).
- A. M. Wodtke and Y. T. Lee, in *Molecular Photodissociation Dynamics*, edited by M. N. R. Ashfold and J. E. Baggot, Vol. 1, pp. 31–59. Royal Society of Chemistry, London (1987).
- J. W. Hepburn, in *Atomic and Molecular Beam Methods*, edited by G. Scoles, D. Laine and U. Valbusa, Vol. 2, pp. 261–288. Oxford University Press, New York (1992).
- A. G. Brenton, *J. Mass Spectrom.* **30**, 657 (1995).
- L. Schnieder, W. Meier, K. H. Welge, M. N. R. Ashfold and C. M. Western, *J. Chem. Phys.* **92**, 7027 (1990).
- J. Segall, Y. Wen, R. Lavi, R. Singer and C. Wittig, *J. Phys. Chem.* **95**, 8078 (1991).
- L. Schnieder, K. Seekamp-Rahn, E. Wrede and K. H. Welge, *J. Chem. Phys.* **107**, 6175 (1997).
- A. T. J. B. Eppink and D. H. Parker, *Rev. Sci. Instrum.* **68**, 3477 (1997).
- R. N. Zare and D. R. Herschbach, *Proc. IEEE* **51**, 173 (1963).
- R. N. Zare, *Mol. Photochem.* **4**, 1 (1972).
- J. C. Brenot and M. Durup-Ferguson, in *State-Selected and State-to-State Ion-Molecule Reaction Dynamics, Part 1: Experiment*, edited by C. Y. Ng and M. Baer, pp. 309–399. Wiley, New York (1992).
- K. Birkinshaw, *J. Mass Spectrom.* **32**, 795 (1997).
- R. N. Bracewell, *The Fourier Transform and Its Applications*. McGraw-Hill, New York (1986).
- H. Helm and P. C. Cosby, *J. Chem. Phys.* **86**, 6813 (1987).
- L. D. A. Siebbeles, J. M. Schins, W. J. van der Zande, J. Loss and M. Glass-Maujean, *Phys. Rev. A* **44**, 343 (1991).
- D. R. Cyr, D. J. Leahy, D. L. Osborn, R. E. Continetti and D. M. Neumark, *J. Chem. Phys.* **99**, 8751 (1993).
- P. Jukes, A. Buxey, A. B. Jones and A. Stace, *J. Chem. Phys.* **106**, 1367 (1997).
- M. J. Van Stipdonk, E. A. Schweikert and M. A. Park, *J. Mass Spectrom.* **32**, 1151 (1997).
- J. A. Betts, Thesis, California Institute of Technology (1971).
- R. D. Clear, S. J. Riley and K. R. Wilson, *J. Chem. Phys.* **63**, 1340 (1975).
- R. Schmiedl, H. Dugan, W. Meier and K. H. Welge, *Z. Phys. A* **304**, 137 (1982).
- G. N. A. van Veen, K. A. Mohamed, T. Baller and A. E. de Vries, *Chem. Phys.* **80**, 113 (1983).
- Z. Xu, B. Koplitz and C. Wittig, *J. Chem. Phys.* **90**, 2692 (1989).
- R. S. Mulliken, *Phys. Rev.* **51**, 310 (1937).
- I. Levy and M. J. Shapiro, *J. Chem. Phys.* **89**, 2900 (1988).
- R. S. Riley and K. R. Wilson, *Faraday Discuss. Chem. Soc.* **53**, 132 (1972).
- G. N. A. van Veen, T. Baller, A. E. de Vries and N. J. A. van Veen, *Chem. Phys.* **87**, 405 (1984).
- D. Imre, J. L. Kinsey, A. Sinha and J. Krenos, *J. Phys. Chem.* **88**, 3956 (1984).
- R. Ogarzalek Loo, H.-P. Haerri, G. E. Hall and P. L. Houston, *J. Chem. Phys.* **90**, 4222 (1989).
- D. W. Chandler, M. H. M. Janssen, S. Stolte, R. N. Strickland, J. W. Thoman, Jr and D. H. Parker, *J. Phys. Chem.* **94**, 4839 (1990).
- D. W. Chandler, J. W. Thoman, Jr, M. H. M. Janssen and D. H. Parker, *Chem. Phys. Lett.* **156**, 151 (1989).
- R. L. Miller, A. G. Suits, P. L. Houston, R. Toumi, J. A. Mack and A. M. Wodtke, *Science* **265**, 1831 (1994).
- A. J. R. Heck, R. N. Zare and D. W. Chandler, *J. Chem. Phys.* **104**, 3399 (1996).
- A. J. R. Heck, R. N. Zare and D. W. Chandler, *J. Chem. Phys.* **104**, 4019 (1996).
- T. Droz-Georget, M. Zyrianov, H. Reisler and D. W. Chandler, *Chem. Phys. Lett.* **276**, 316 (1997).
- A. Sanov, T. Droz-Georget, M. Zyrianov and H. Reisler, *J. Chem. Phys.* **106**, 7013 (1997).
- F. Harren, D. H. Parker and S. Stolte, *Comments At. Mol. Phys.* **26**, 109 (1991).
- J. W. G. Mastenbroek, C. A. Taatjes, K. Nauta, M. H. M. Janssen and S. Stolte, *J. Phys. Chem.* **99**, 4360 (1995).
- M. H. M. Janssen, J. W. G. Mastenbroek and S. Stolte, *J.*

- Phys. Chem. A* **101**, 7605 (1997).
61. D. H. Parker, Z. W. Wang, M. H. M. Janssen and D. W. Chandler, *J. Chem. Phys.* **90**, 60 (1989).
 62. D. Y. Kim, N. Brandstater, L. Pipes, T. Garner and D. Baugh, *J. Phys. Chem.* **99**, 4364 (1995).
 63. M. Guilhaus, *J. Mass Spectrom.* **30**, 1519 (1995).
 64. A. T. J. B. Eppink, D. H. Parker, M. H. M. Janssen, B. Buijsse and W. J. van der Zande, *J. Chem. Phys.* **108**, 1305 (1998).
 65. A. G. Suits, R. L. Miller, L. S. Bontuyan and P. L. Houston, *J. Chem. Soc., Faraday Trans.* **89**, 1443 (1993).
 66. H. Katayanagi, Y. Mo and T. Suzuki, *Chem. Phys. Lett.* **247**, 571 (1995).
 67. T. Suzuki, H. Katayanagi, Y. X. Mo and K. Tonokura, *Chem. Phys. Lett.* **256**, 90 (1996).
 68. D. W. Chandler, D. W. Neyer and A. J. R. Heck, SPIE Proceedings 3271, Laser Techniques for State Selected and State-to-State Chemistry IV, J. W. Hepburn, R. E. Continetti and M. A. Johnson (eds), in press (1998).